

Development of Requirements for Resistance Spot Welding Dual-Phase (DP600) Steels

Part 1 — The Causes of Interfacial Fracture

Weld fracture was investigated in relation to weld parameters and steel sheet characteristics

BY M. MARYA and X. Q. GAYDEN

ABSTRACT. The resistance spot welding of two galvanized DP600 steels with 1.8 and 2.0-mm sheet thickness was investigated to enhance our understanding of weld fracture during a well-established automotive quality control test. The effects of several process parameters (including weld current, weld time, and weld force) on zinc expulsion, mechanical properties, defects, and microstructures of resistance spot welds were all studied in relation with the two major types of weld fracture (i.e., interfacial and button pullout). It was established that the slight differences in chemical composition and galvanized coating between the two selected DP600 steels affected negligibly weld microstructures, and were of no measurable consequences to weld fracture. In contrast, the difference of 10% for their sheet thickness was responsible for smaller weld diameters, lower weld tensile-shear forces, larger shrinkage voids, and more frequent interfacial fractures in welds from the thicker DP600 steel. For the two steels, occurrence of weld interfacial fracture was eliminated using long weld times (>20 cycles), low currents (<9 kA), and high forces (>900 lb, or 4.0 kN); i.e., process parameters that increased weld diameters while preventing zinc ingestion into the fusion zone. The effect of zinc was most prominent in welds that were made abnormally fast (e.g., ~5 cycles), where both solidification cracking and a change in type of weld fracture were found due to in-

terdendritic low-melting point constituents.

Introduction

The drive for vehicle mass reduction has led to the introduction of new engineering materials. The Ultra Light Steel Auto Body (ULSAB) project has shown that car body mass can be reduced by 25% using advanced high-strength steels (AHSS) and innovative processes (Ref. 1). Among the AHSS, the dual-phase (DP) steels have been the subject of particular attention owing to their good combination of high strength and ductility. The term dual-phase steel refers to the predominance of two phases, the body-centered-cubic (bcc) α -ferrite and the relatively harder body-centered-tetragonal (bct) martensite. These two phases are produced by some annealing in the A_1 - A_3 "intercritical" temperature, where austenite and ferrite are formed, and a subsequent rapid cooling where the austenite is eventually transformed into martensite. Since suitable amounts of ferrite and martensite in DP steels may be produced from a combination of heat-treating parameters, compositions of DP steels may vary significantly between steel makers, as

found in Part 2 of this study (Ref. 4) to be published in the near future. To create yield strengths of 350 MPa and ultimate strengths of 600 MPa, the DP600 steels (as commonly referred by the ULSAB Consortium.) (Ref. 1) were all found to possess about 15% martensite. Compared to precipitation-strengthened or solid-solution-strengthened HSLA steels, DP600 steels exhibit a slightly lower yield strength, a continuous yield behavior due to enough active slip systems in the ferrite phase, and a more uniform and higher total elongation (over 21%) (Refs. 1, 2). These last two properties explain their relatively good formability; a property, which combined with their high strengths, has made DP steels attractive for automotive applications (Refs. 1-3).

The acceptance of DP steels in manufacturing environments has been extremely gradual though DP steels offer evident advantages, and they have demonstrated a good weldability (Refs. 3, 5-8). However, on automotive factory floors and in testing laboratories, the definition for weldability can differ, and so are the tests and criteria used to differentiate "good" welds from "bad" welds. In the simplest of all quality-control tests, a handheld chisel is inserted in between spot-welded coupons to force the welds to fracture, and, based upon a visual inspection, determine if the same welds would be appropriate in vehicle applications (Ref. 9). In early chisel tests, spot welds in DP600 steels had been found to underperform welds in traditional automotive steels; i.e., non-AHSS (Ref. 1) (e.g., interfacial-free steels, low-carbon steels, rephosphorized steels, mild steels, or HSLA steels). Especially with the thicker DP600 steel gauges, welds were seen to fracture in the same plane as the sheet sur-

KEYWORDS

Automotive Steels
Dual-Phase (DP600)
Resistance Spot Welding
Properties
Microstructures
Defects

M. MARYA, formerly with G. S. Ansell Department of Metallurgical and Materials Engineering, Colorado School of Mines, Golden Colo., is now with NanoCoolers, Inc., Austin, Tex. X. Q. GAYDEN is with Materials and Process Laboratory, General Motors Research and Development, Warren, Mich.

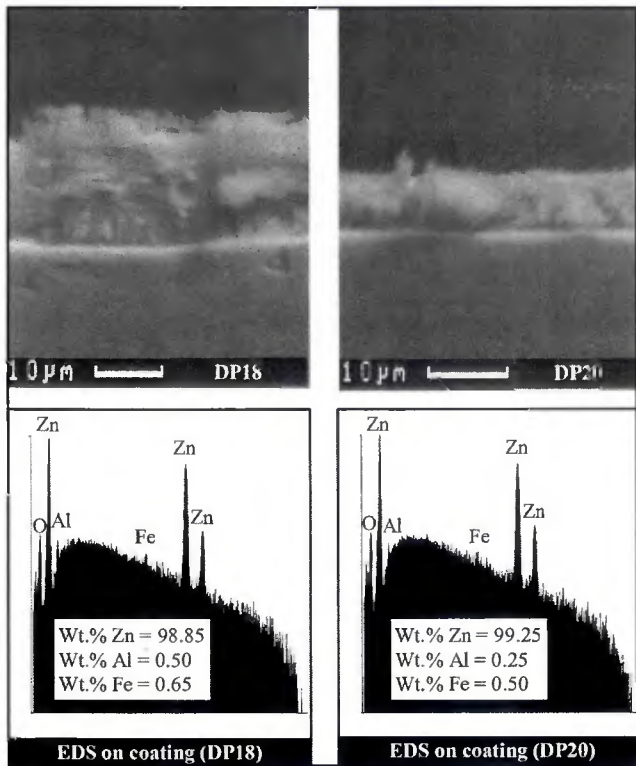


Fig. 1 — Secondary electron images showing the galvanized layers on the two DP600 steels and electron dispersive spectra indicating their approximate chemical compositions.

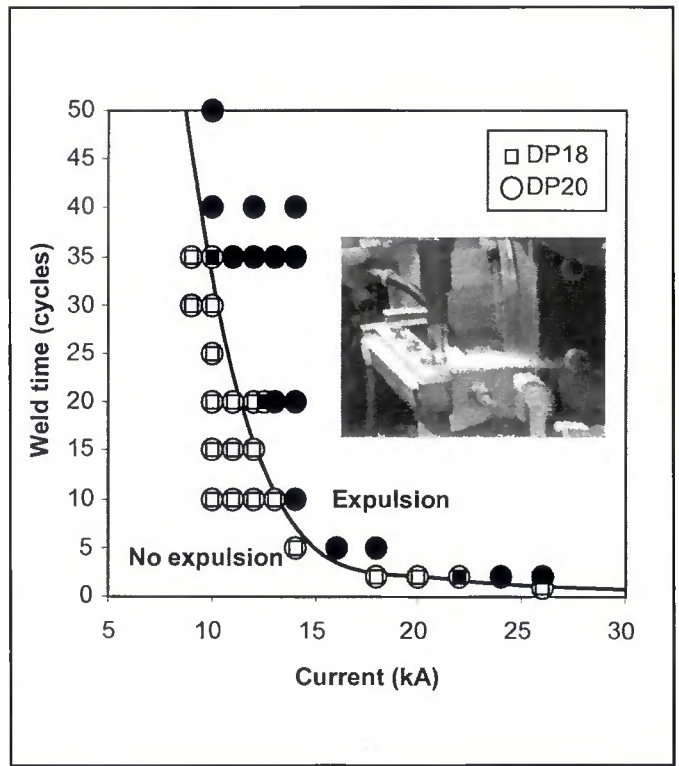


Fig. 2 — Process map describing the effects of the current and weld time on zinc expulsion for both DP18 and DP20 (1200-lb weld force).

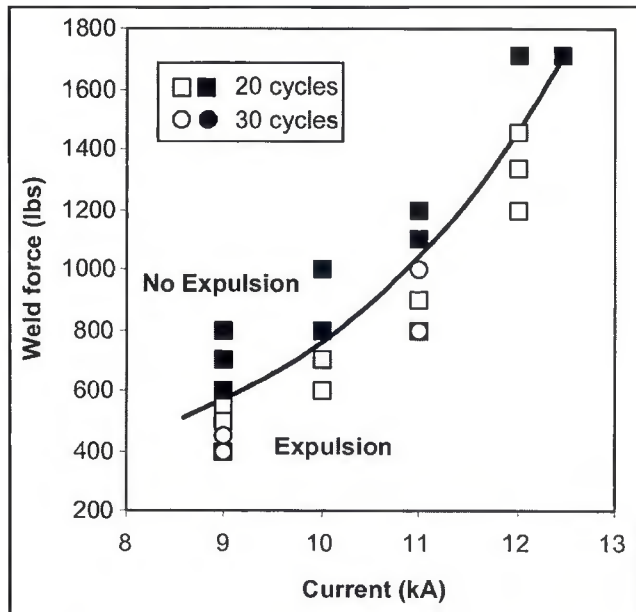


Fig. 3 — Process map describing the effects of the weld force on the zinc expulsion for the DP20 steel (1200-lb weld force).

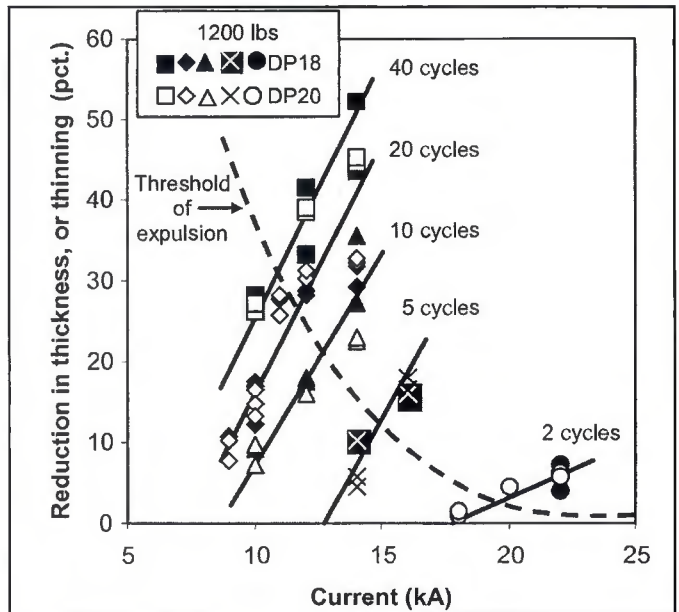


Fig. 4 — Reduction in thickness or thinning vs. current and weld time for welds made in DP18 and DP20 steels (1200-lb weld force).

faces, causing the so-called "interfacial fracture." The occurrence of weld interfacial fractures in DP600 steels was in contrast with the traditional automotive steels, where weld fracture is known to occur consistently in the fusion zone periphery, promoting the so-called "weld

button." For spot welds to be reliable during vehicle lifetime, they are required to tear a button during quality control. The formation of a weld button during quality control indeed indicates that the same weld would have been able to transmit a high level of force, thus cause severe plas-

tic deformation in its adjacent components, and increased strain energy dissipation in crash conditions.

In Part I of this investigation on the weldability of DP600 steels in production environments, fracture in spot welds from two commercial steels was induced mainly

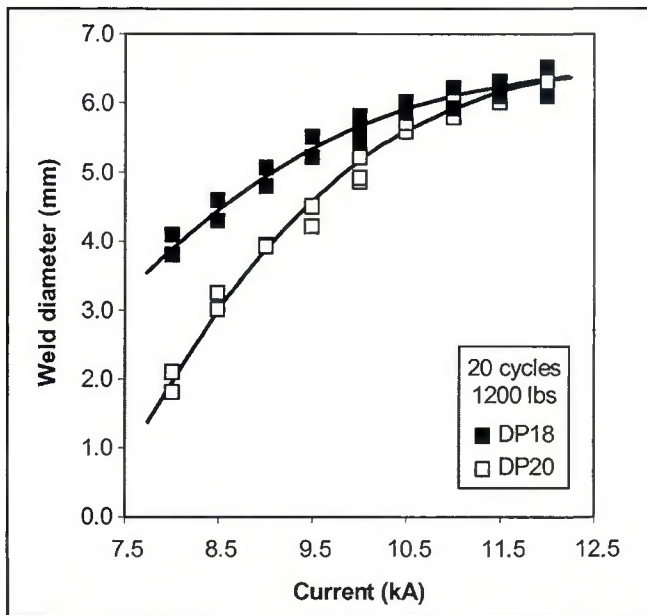


Fig. 5 — Weld diameter (as measured after peeling) vs. current for welds made in DP18 and DP20 steels (20-cycle weld time and 1200-lb weld force).

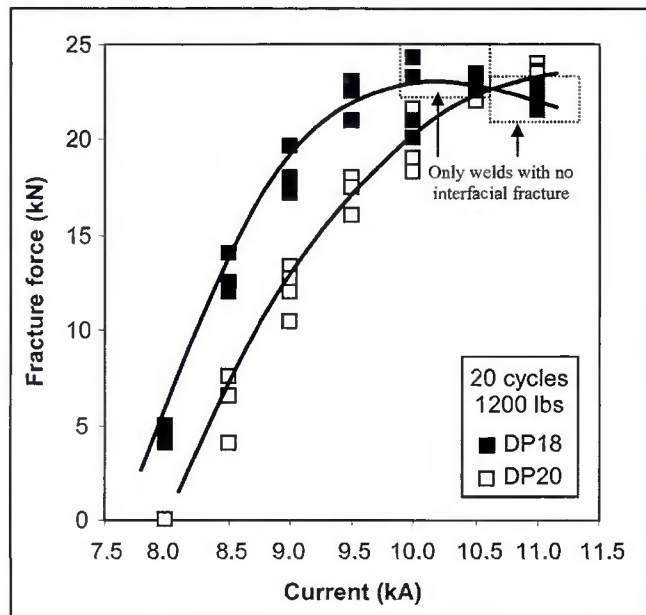


Fig. 6 — Fracture force (peak force recorded during tensile-shear testing) vs. current for spot welds made in DP18 and DP20 steels (20-cycle weld time and 1200-lb weld force).

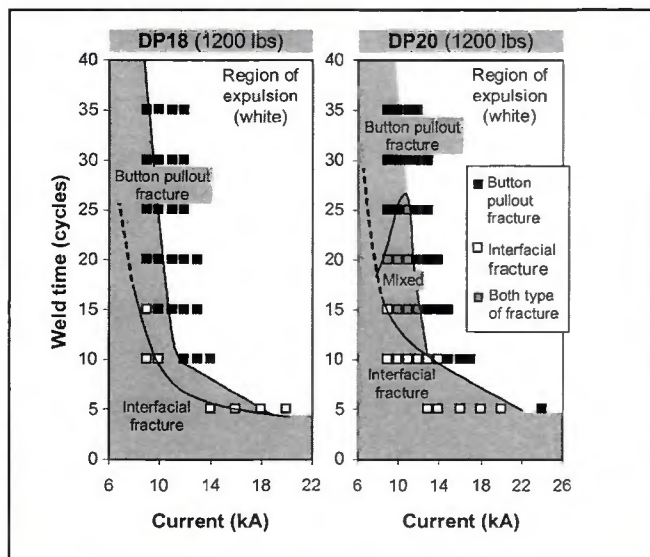


Fig. 7 — Process maps showing effects of both current and weld time on the type of weld fracture encountered during chisel testing on DP18 (left) and DP20 (right) steels (1200-lb weld force).

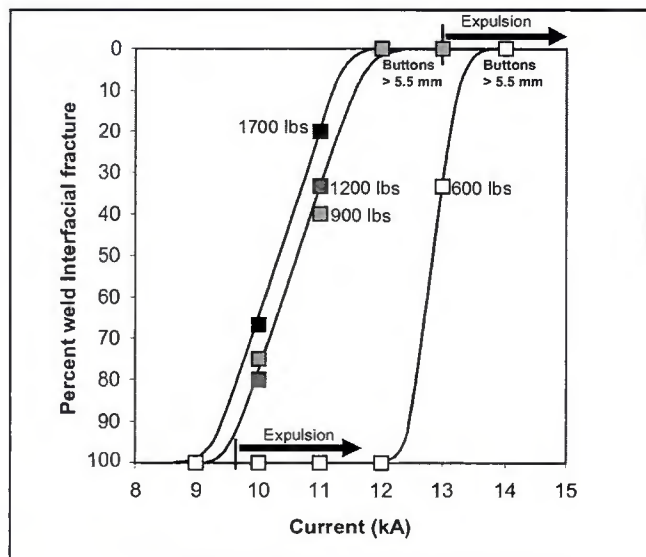


Fig. 8 — Percent weld interfacial fracture vs. current and force for spot welds made on DP20 (20-cycle weld time).

by the chisel test (Ref. 9). When this study was initiated in 2003, it was primary to first establish a relationship between process parameters and occurrence of weld interfacial fracture using a minimum of two DP600 steels. Since weld diameter is well-known to be a key player in weld fracture (Refs. 6, 9–14), weld diameters were measured and correlated to the process parameters, as were the weld microstructures. In this first study, the weld microstructures were thoroughly examined due to well-

established relationships with the mechanical properties, and thus fracture (Refs. 5–8). In this article, the reader will discover that the weld microstructures are first discussed and linked to the steel compositions, as suggested by the Nippon Steel carbon equivalent (CE) here presented as Equation 1 (Refs. 12–14). This CE, developed from non-AHSS spot welds that were quasi-statically cross-tension tested (Refs. 12–14), connects chemical composition with one of the two

types of weld fracture. This CE, yet unproven for AHSS steels, presented a means for measuring DP steel spot weldability with a load orientation that was not too different from the chisel test load orientation. Equation 1 for this CE infers that a relatively hard and brittle weld (i.e., one that is made of martensite) having enough sulfur and phosphorus (i.e., elements that segregate to boundaries and increase solidification cracking susceptibility, Refs. 15, 16) will fail interfacially

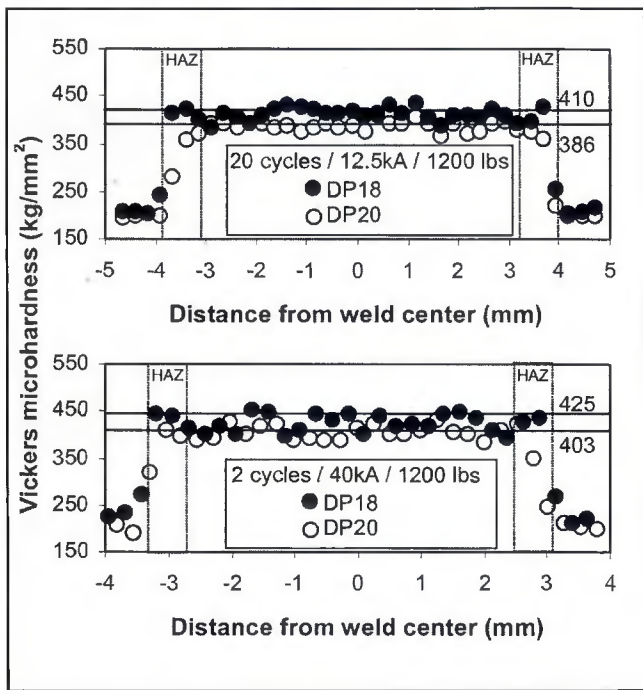


Fig. 9 — Microhardness profiles for welds in DP18 and DP20 produced using widely different welding conditions (microhardness was measured using a 200-g load and 30- μ m away from the weld centerline).

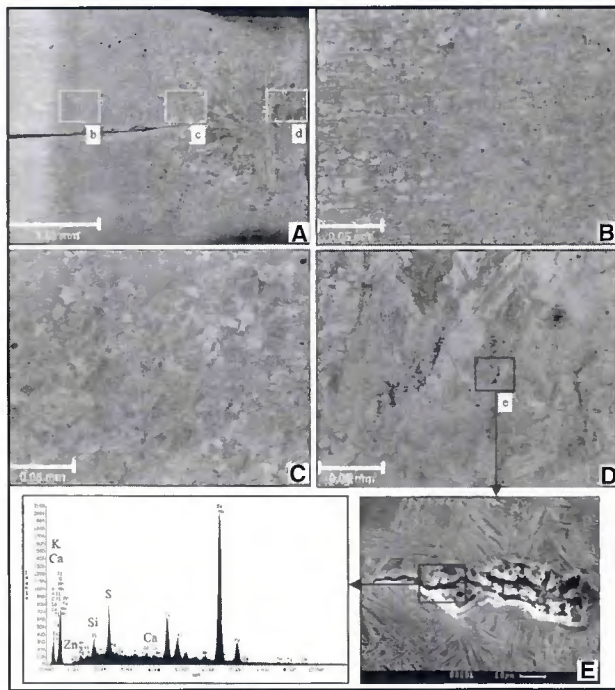


Fig. 10 — Optical micrographs of microstructures in a spot weld made in DP20 steel (12-kA current and 20-cycle weld time), and EDS results revealing the presence of nontransition metals, including sulfur.

during testing if CE is greater than 0.24 (Refs. 12–14).

$$CE|_{0.24\text{limit}} = C + \frac{Si}{30} + \frac{Mn}{20} + 2P + 4S \quad (1)$$

Although not detailed here, but suggested elsewhere (Ref. 14), zinc contamination from the coatings is also another potential contributor to weld fracture. Consequently, the effects of process parameters, sheet thickness, steel composition, and coating were all important to consider for fully explaining the weldability of DP600 steels, since they all influence weld dimensions, weld microstructures, and weld mechanical properties, including fracture characteristics (Refs. 4–19).

Experimental Procedure

Materials

Following suggestions by manufacturing engineers, two hot-dipped galvanized DP600 steels of commercial availability were selected with two distinct gauges. The thinner steel, designated as DP18, was 1.8 mm thick, whereas the second, DP20, was supplied in a 2.0-mm sheet thickness. For testing, the steel sheets were sheared into 38 \times 127-mm coupons. Guided by Equation 1, the steel chemical compositions were precisely measured

and verified using a combination of techniques: X ray fluorescence (XRF), inductively coupled plasma (ICP) spectroscopy, and wavelength dispersive spectroscopy (WDS).

Welding

All resistance spot welds were fabricated using a mid-frequency DC welding machine, where current was delivered through C15000 Cu-Zr alloy caps with a 5.0-mm face diameter. To minimize weld-to-weld variations introduced by cap wear, the caps were regularly inspected using reference welds, which were generated each time new caps were inserted. These reference welds were all produced using typical process parameters (e.g., 9 kA, 20 cycles and 1200 lb, or 5.3 kN).

When the repeat of a reference weld with used caps resulted in a weld with a new diameter and type of weld fracture, new caps were systematically mounted. This precaution guaranteed that the welding con-

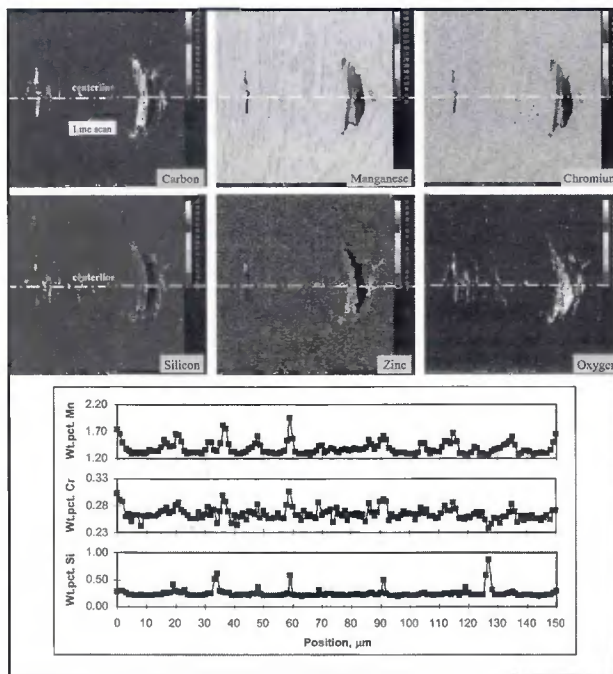


Fig. 11 — X-ray compositional maps near the center of an unetched spot weld made in DP20 steel (12.5 kA current and 20-cycle weld time) with line scans for three alloying elements, all revealing some microsegregation.

ditions were not drifting over time, and that the two steels could be compared under identical conditions at any time if needed.

Each welded sample was made of two

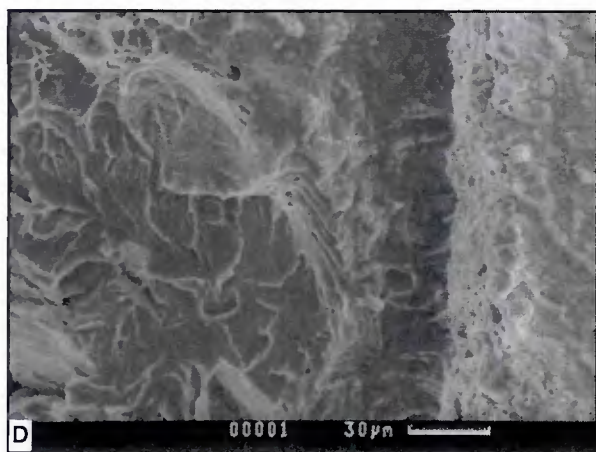
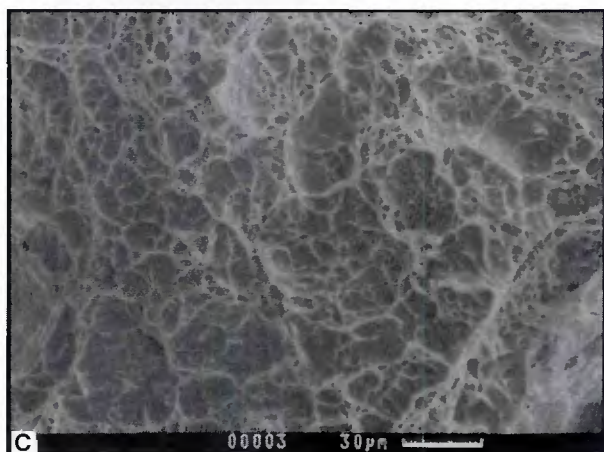
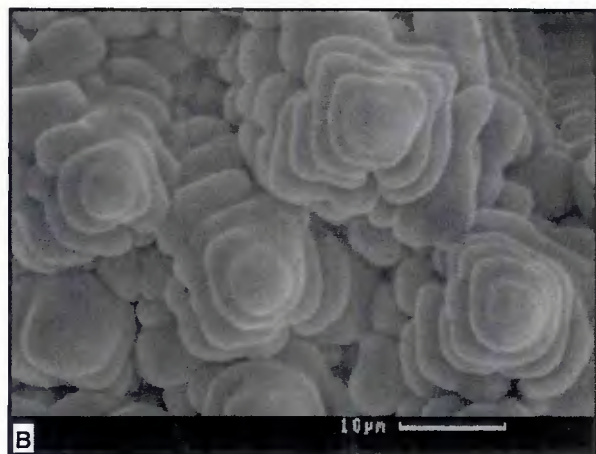
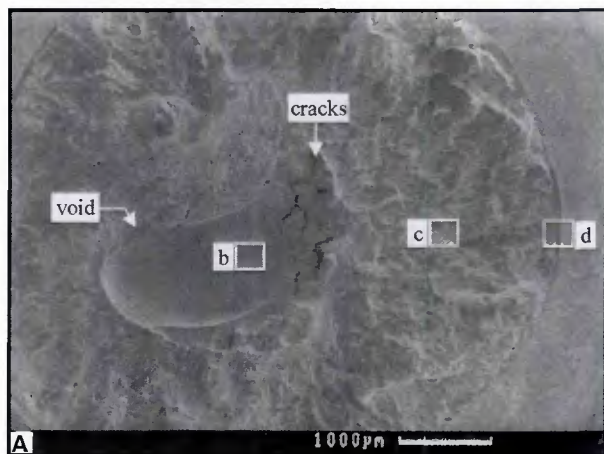


Fig. 12 — Secondary electron images of an interfacially failed spot weld in DP20 steel (12 kA current, 10-cycle weld time, 1200 lb weld force).

Table 1 — Measured Chemical Composition of the Two DP600 Steels (wt-%) with CE, as Defined by Equation 1

	C	Mn	Cr	Mo	Ni	Ti	V	Al	Si	P	S	B	N	O	CE
DP18	0.13	1.40	0.21	0.05	0.02	0.01	<0.01	0.02	0.4	0.02	<0.002	<0.001	0.0051	0.0025	0.253
DP20	0.11	1.50	0.27	<0.005	0.02	<0.005	0.06	0.06	0.1	0.02	<0.003	<0.001	0.0065	0.0028	0.228

identical coupons. On each, three spot welds, separated by about 35 mm, were produced. Weld current and weld time were varied between 7 and 40 kA and between 2 and 40 cycles, respectively. The weld force (i.e., the compressive force induced by the electrodes) was applied 90 cycles before the current, and lasted 5 cycles longer. Although several force levels were selected, primarily to differentiate the two DP600 steels, the weld force was preferentially held at 1200 lb (5.3 kN).

Property Measurements

The overwhelming majority of the welded samples was either peeled to force the formation of weld buttons and measure their diameters, or chisel-tested to

identify the predominant type of fracture (Refs. 9, 10). Other welded samples were tensile-sheared at a low-crosshead velocity of 4 mm/min to precisely capture and quantify weld static characteristics. This test was preferred over cross-tension and coach-peel tests because of greater data reproducibility, reliability, and accuracy; all necessary to compare the two DP600 steels. For tensile-shear testing, the welds were centered in the overlap section, which like the coupon width was 38-mm long. The same test configuration is described in other studies (Refs. 5, 6).

Several welds were cross-sectioned, cold-mounted, ground, and polished with carbide paper, diamond paste, and fine colloidal silica. The microstructures were then revealed by etching with a 2% nital

reagent and examined by optical and scanning electron microscopy (SEM). Chemical compositions, including high-resolution mapping, were measured using electron/wavelength dispersive spectroscopy (EDS/WDS). The Vickers microhardness under a 200-g load was also measured, and linked to the observed microstructures.

Results and Discussion

Base Material Characteristics

Measured chemical compositions, summarized in Table 1, show that the DP18 steel had slightly more carbon than the DP20 steel. This greater carbon content of DP18 appeared to counterbalance a rel-

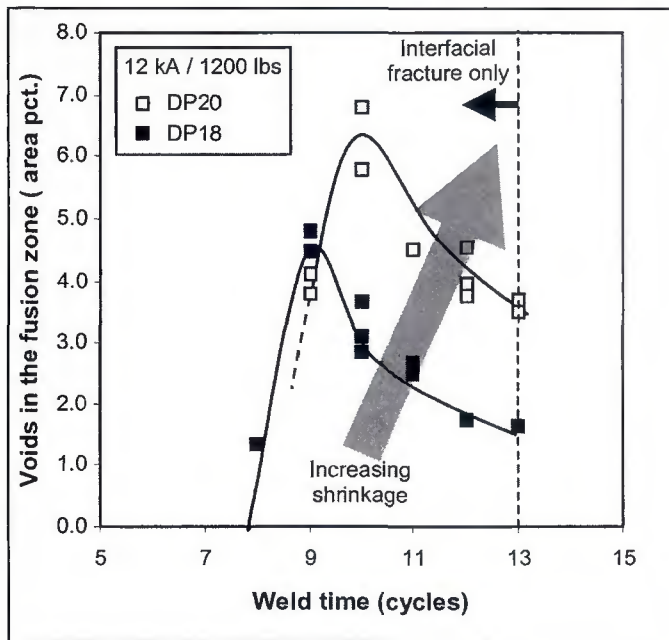


Fig. 13—Percent voids in weld fusion zones vs. weld time for spot welds made in DP18 and DP20 steels (12-kA current and 1200-lb weld force).

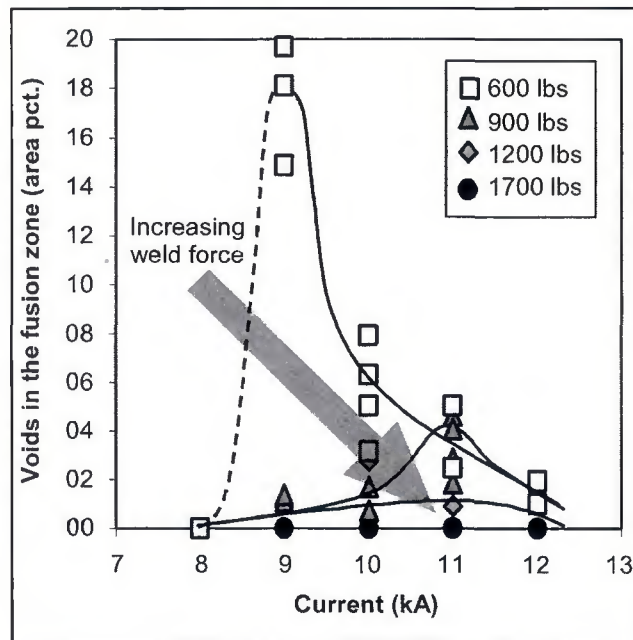


Fig. 14—Percent voids in weld fusion zones vs. current and weld force for spot welds made in DP20 steel (20-cycle weld time).

ative shortfall of strengthening elements such as manganese, chromium, and vanadium. In both DP18 and DP20, the boron contents were also less than 10-wt-ppm; a concentration that therefore neither could increase steel hardenability (Ref. 17) nor cracking susceptibility (Ref. 14).

Table 1 provides the carbon equivalents for DP18 and DP20. Although the CE was determined with Equation 1 that normally applies to non-AHSS steels (Refs. 12–14), the CE could still be utilized as a relative indicator of hardenability and weldability. Since the CE for both steels was close to the limit of 0.24, variability in the types of weld fracture was expected to be greater than in non-AHSS steels, where the CE is typically smaller. Also, note that the carbon equivalent of DP18 not only exceeded that of DP20, but also the value of 0.24 given by Equation 1 (Refs. 12–14). Consequently, with only the CE to describe weld fracture, the spot welds in DP18 could have been expected to fracture interfacially more frequently than in DP20. The question as to whether this statement is correct or not is answered later in this paper.

As for the as-received microstructures (not shown), they were comparable in DP18 and DP20. Both steels had average grain sizes of about 10 μm and contained approximately 15% martensite. However, hardness of the DP18 steel was greater than that of DP20, averaging 205 kg/mm^2 vs. 185 kg/mm^2 for the DP20 steel. Coincidentally or not, this difference in hardness

agrees with the CE values.

SEM observations revealed that the galvanized layer was 9 μm thick in DP20 and nearly twice as thick in DP18 (Fig. 1), while EDS and XRF measurements showed that coating compositions were similar with at least 99 wt-% zinc and less than 1 wt-% aluminum. Therefore, the possibility that coating compositions affected weld fracture in the two DP600 steels could be eliminated.

Spot Weld Expulsion

In the resistance spot welding of galvanized steels, the expulsion of zinc (i.e., the element that melts and vaporizes first) is important to examine, as it limits the selection of the process parameters. Zinc can be expelled both at the electrode-sheet interfaces, and at the interface between the two sheets where the weld forms (Refs. 18–20). Due to water cooling within the electrodes, the temperature is normally greater at the interface between the sheets and expulsion occurs there first (Ref. 18). Because this expulsion is more difficult to detect when it first occurs, only the expulsion from the electrode-sheet interface is considered here.

Figure 2 describes the effects of weld current and weld time on zinc expulsion. To determine with precision the threshold of zinc expulsion for the two steels, each data point was generated from at least three welds. Judging from Fig. 2, the possibility that the thicker zinc coating of

DP18 (Fig. 1) could have promoted more expulsion was ruled out since a single boundary between the expulsion-free and the expulsion regions was found for the two steels. Although both DP18 and DP20 were indistinguishable here, Fig. 2 was later found to be extremely useful for selecting appropriate process parameters, and to further compare DP18 and DP20.

In Fig. 2, the solid line demonstrates that the current at the beginning of expulsion is inversely related to the weld time. Consequently, to create large welds, current and weld time must be selected such that they are positioned close to this boundary line, and, to prevent expulsion, they must be also on the left of this boundary line. Moreover, to enhance weld process repeatability, the best-controlled variable (i.e., weld time) must be extended as much as possible, whereas the current, the second variable of Fig. 2, must be minimized to alleviate its relative contribution in the weld formation, and to prevent extensive cap wear (Ref. 6). Unlike the weld time, the current is self-regulated and varies as contact resistance, material properties, alignment, and cap wear gradually change from one weld to another (Refs. 6, 15, 18–20). For this study, where a high level of reproducibility between welds was needed to compare DP18 and DP20, extended weld times (> 20 cycles) and correspondingly small currents (<9 kA) were particularly appropriate.

Figure 3 is a complementary figure describing weld force effect on zinc expul-

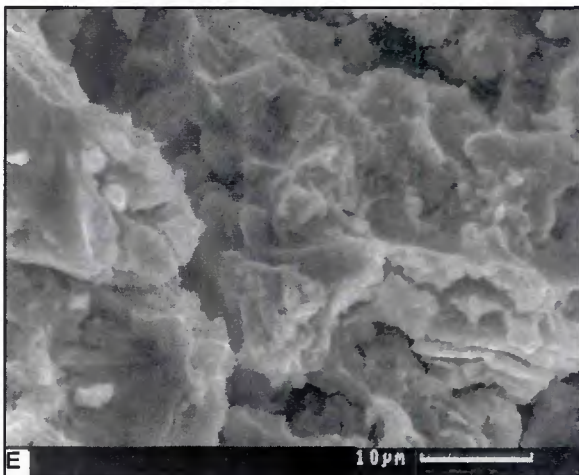
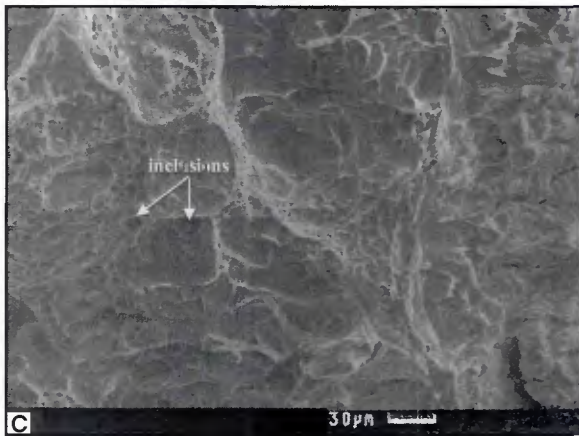
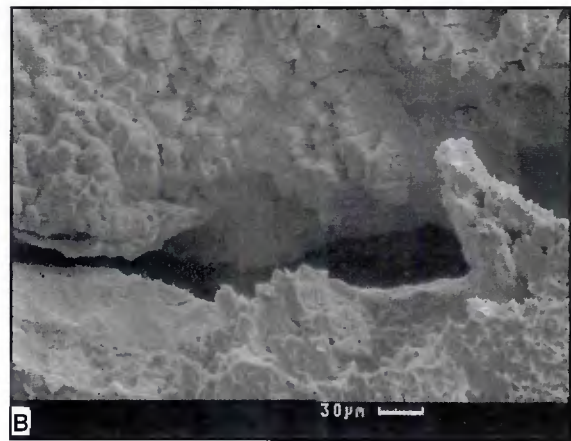
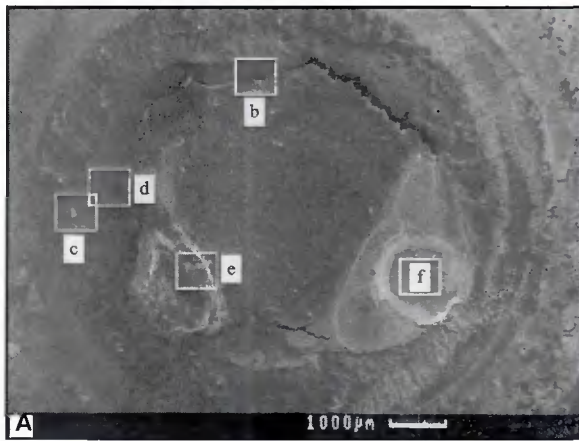


Fig. 15 — Secondary electron images of a spot weld produced using unusual process parameters (24-kA current, 5-cycle weld time, 1200-lb weld force). Weld button formation appeared to be promoted by zinc ingestion.

sion with weld times of 20 and 30 cycles. For currents of 12 kA and less, zinc expulsion was prevented by reasonably low-weld forces. In contrast, the currents over 12 kA were found to be impractical as the required forces to prevent expulsion were then too high for many industrial welding machines. Despite this new constraint, we

occasionally selected currents of 12 kA and higher, as justified later.

Weld Joint Properties

Spot Weld Morphology

In addition to preventing zinc expulsion,

the compressive force applied by the electrodes forges the fused region to a thinner gauge. Such thinning caused by indentation can alter spot weld properties, as quantified in a recent study (Ref. 21), and was therefore another factor guiding the selection of the process parameters. For a weld force of 1200 lb (5.3 kN), Fig. 4 de-

scribes current and weld time effects on the thinning seen across more than 60 spot welds from DP18 and DP20. Exactly like in Fig. 2, the results for both DP18 and DP20 were nearly identical. In Fig. 4, note that we superimposed a dash line to show regions of expulsion and no expulsion (left to the dash line). At the onset of expulsion, thinning never exceeded 30%, and was less than 20% for most welds. With this limited indentation, numerous studies have shown that the indentation effect is negligible compared to that of weld diameter (Refs. 15, 20, 21). Consequently, the effect of process parameters on weld diameter (measured after peeling to promote weld buttons) had to be examined before a link with the types of weld fracture could be researched.

Figure 5 shows that weld (button) diameter increases with the current at a rate that is gradually and monotonically decreasing, as observed elsewhere (Refs. 20, 22–24). When the current exceeded 11 kA, the weld button diameters in both steels stabilized slightly above 6.0 mm. At lower currents, the welds were noticeably larger in DP18, particularly when button diameters were less than 5.5 mm. This result revealed that welds in DP18 formed at lower heat inputs than in DP20, and that could be reasonably well explained by the fact that DP18 was 10% thinner than DP20. With thickness emerging as the main explanation for the discrepant weld diameters in DP18 and DP20, we were expecting a number of spot welds from DP18 and DP20 to exhibit different types of fracture, even with identical process parameters. The effects of process parameters on weld mechanical properties, including types of weld fracture, were therefore important to clarify, first under well-controlled conditions, and then using the chisel test; i.e., as if welds were quality controlled on factory floors.

Tensile-Shear Test Results

Many welds, fabricated with identical parameters as in Fig. 5, were tensile-sheared to quantify their load-carrying capabilities, and, despite loading conditions different than in the chisel test, determine if one steel was also more prone to spot weld interfacial fracture than the other. In Fig. 6, peak force recorded during testing (i.e., the weld fracture force) is represented as a function of current. Figure 6 shows that the weld fracture forces were consistently greater in DP18. Although the trend lines for the two steels were alike, the trend line for DP18 was also shifted to the left of that for DP20; a confirmation that the welds began to form at smaller currents in DP18, and that the

greater fracture forces seen in the welds of DP18 were primarily due to its thinner gauge.

Among the welds in Fig. 6, six out of the 38 (all in DP18) created buttons. With several, the fracture forces were seen to reach a maximum at intermediate currents (i.e., 10 to 10.5 kA). At these currents, interfacial fracture was also seen to fully disappear. With a further increase in current, interfacial fracture continued to be avoided, but the sheets were also alarmingly indented. As confirmed by Fig. 4, with currents near 10 kA, thinning across welds was about 20%. For the welds produced with greater currents, thinning not only exceeded 30%, but the welds were also observed to form buttons along the indentation. The possibility that indentations over 20 to 30% influenced weld fracture during tensile-shear testing, and especially during chisel testing, was therefore raised.

Quality (Chisel) Test Results

Figure 7 compares chisel test results for spot welds also made with a 1200-lb (5.3 kN) force. The two types of fracture, interfacial (white squares) and button-pullout (black squares), are mapped as a function of current and weld time. Since each data point was generated by testing 3 to 12 welds depending upon the observed repeatability, results from more than 400 welds are summarized in Fig. 7. While both steels exhibit regions where only a single type of fracture occurred, the DP20 steel is characterized by having a region with the two types of weld fracture. This region is bound by currents between about 10 and 14 kA and weld times between about 15 and 25 cycles. As currents and/or weld times were increased, the percentage of each type of fracture varied from zero to one hundred, and vice versa. For DP20, interfacial fracture was also found to vanish when expulsion started. Of these two observations, the first indicated that the chisel test was largely reproducible, and the second inferred that zinc expulsion was potentially related to weld fracture, as hypothesized previously.

To determine if zinc expulsion had influenced the type of weld fracture, some welds were produced by varying currents and forces, which, as seen in Fig. 3, both affect expulsion remarkably well. The welds, made with selected forces of 600 lb (2.7 kN), 900 lb (4.0 kN), 1200 lb (5.3 kN), and 1700 lb (7.6 kN), were subsequently chisel tested, and correlations between type of weld fracture and occurrence of expulsion were searched. The results of these tests are summarized in Fig. 8, where percentage of a given type of weld fracture

is represented as a function of current and force. For a given force, Fig. 8 shows that the occurrence of weld interfacial fracture gradually decreased with the current. More specifically, at 600 lb (2.7 kN), expulsion of zinc started before the current could be raised high enough to fully eliminate interfacial fracture. In contrast, at 1700 lb (7.6 kN), zinc expulsion was detected after interfacial fracture had been prevented. For the process conditions of Fig. 8, it became clear that zinc expulsion was not primarily related to weld fracture, and the common boundary in Fig. 7 for the regions of mixed fracture and expulsion could only be coincidental.

Figure 8 also points out that the high weld forces reduced the minimum current to prevent interfacial fracture. Indeed, once weld force exceeded 900 lb (4.0 kN), weld buttons were produced at smaller currents (10 kA vs. 12.5 kA at 600 lb, or 2.7 kN). This result confirmed that the level of applied force affected weld formation, presumably by affecting contact area and contact electrical resistance (Refs. 18–20, 24, 25). Since Fig. 8 also shows that weld current was negligibly affected by forces over 900 lb (4.0 kN), we concluded in agreement with another study (Ref. 19) that the contact resistances were practically unchanged once a certain force, or pressure, is exceeded.

In Fig. 8, also note that the minimum weld diameter to eliminate interfacial fracture was consistently in the vicinity of 5.5 mm regardless of weld force and current. This 5.5-mm value, measured after chisel testing, was confirmed by some of the test data presented earlier. For currents of 9 and 10 kA, Fig. 7 showed that weld interfacial fracture fully disappeared once weld times exceeded 25 cycles in DP18 and about 30 to 35 cycles in DP20. With these process parameters, Fig. 5 then revealed that interfacial fracture would not occur for weld button diameters over 5.5 mm in DP18 and 6.0 mm in DP20. Based upon this analysis and the data of Fig. 8, we therefore confirm that some minimum weld diameters could be recommended to prevent weld interfacial fracture, as further investigated in Part II of this work (Ref. 4).

As complementary remark resulting from a comparison of Figs. 6, 7, and 8, note that many of the tensile-sheared welds of Fig. 6 that fractured interfacially would have produced buttons if instead they would have been chisel tested. This demonstrates that the chisel test is less selective than the quasi-static tensile-shear test, and that any weld identified as a “good” weld by the tensile-shear test would also be a “good” weld if tested in production using the chisel test.

Weld Heterogeneity

To complete this study, metallurgical analyses were needed in view of various opinions that came to us. We had to determine if differences other than sheet thickness explained the greater susceptibility of DP20 toward weld interfacial fracture. Since steel chemical composition first appeared to be important (Equation 1), variations in hardness (i.e., strength), microstructure, and local composition were examined to attempt determining all causes, primary or secondary, of spot weld fracture in DP600 steels.

Variations in Microhardness

For both DP18 and DP20, Fig. 9 depicts microhardness profiles for welds produced with both regular and unusually fast welding schedules (12.5 kA, 20 cycles vs. 40 kA, 2 cycles). The average hardness values of the weld fusion zones are also shown by the horizontal straight lines. Average hardness was higher in the rapidly-made high-current weld, as seen by comparing the upper and lower graphs. Also, for all welds, microhardness fluctuated slightly and always peaked in the HAZ, marked as HAZ. Near the fusion zone, where microstructure was the hardest, hardness exceeded 400 kg/mm² and was about twice greater than in the base material. Like many non-AHSS, which have all consistently produced buttons after chisel testing, no measurable softening was detected near the base metal (Refs. 6, 27). A softening in the HAZ would have helped plastic strain to localize and fracture to follow outside the hard fusion zone (Refs. 27–29). Therefore, this feature alone would have explained why welds in DP600 fracture more interfacially than traditional automotive steels.

Regardless of the welding parameters, the HAZ and the fusion zone were harder in DP18, a result that agrees with the CE values of Table 1. While microhardness in both fusion zone and HAZ were greater in DP18, the hardening with respect to the initial microstructure (or percent increase in hardness) was greater in the welds of DP20. This hardening was 2.17 in DP20 vs. 2.05 in DP18. If comparing strength of fusion zone or HAZ with that of base metal is important, as suggested by mathematical modeling (Refs. 28, 29), then examining hardening was not helpful here in explaining the greater susceptibility of DP20 to weld interfacial fracture, because a greater hardening generally correlates with less interfacial fractures (Ref. 27). If, instead, the CE of Equation 1 is used to differentiate steels by types of spot weld fracture, then CE cannot explain the superior performance of DP18 during chisel

testing. Of all factors, only sheet thickness has to this point explained the dissimilar behavior and different weldability of DP18 and DP20.

Variations in Microstructure

Examination by optical microscopy of weld cross sections neither distinguished DP18 from DP20, but did reveal microstructural features that potentially affected weld fracture in DP18 and DP20. Fig. 10 depicts four optical micrographs of a characteristic spot weld in DP20. The low-magnification micrograph of Figure 10A shows that microstructure was more heterogeneous in the fusion zone than in the HAZ. Figure 10B, for the colder section of the HAZ, demonstrates that its microconstituents were considerably finer than those of either the base metal or the fusion zone (Figs. 10C and 10D). This is explained by the fact that austenitizing was incomplete in the colder section of the HAZ, and even when austenite grains formed, grain growth was restricted by the thermal cycles. In this section of the HAZ where austenite grains are fine, the resulting high density of grain boundaries constitute obstacles against the formation of large martensite laths. As opposed to the coarser martensite of Fig. 10E, observed in the fusion zone, the fine martensite of the HAZ was not well resolved by SEM. As shown in Fig. 9, hardness corresponding to the fine microstructures of the HAZ was also greatest.

Figure 10C shows a region of the fusion zone near the HAZ. Large aggregates of a white blocky phase (presumably ferrite) can be observed in between finer microconstituents. Due to their unique morphology, these fine microconstituents were also identified by SEM as martensite. Figure 10D depicts a narrow view of the fusion zone center. Tiny cracks (approximately 50 μ m long) were regularly seen, especially in the DP20 steel welds. The irregular topography seen in these cracks and revealed by Fig. 10E suggests shrinkage cracks, or solidification cracks; the later being more likely, as indicated by EDS measurements of sulfur, calcium, potassium, and silicon (i.e., many elements that are found in slags for deoxidizing and desulfurizing steel and that are normally removed to minimize solidification cracking tendency) (Ref. 2).

Although all our observations indicate that the role played by microscopic cracks on weld fracture is unlikely significant compared to that of the sheet thickness, this section has brought another explanation for the greater susceptibility of DP20 for weld interfacial fracture. These microscopic cracks, most distinctively encountered in the DP20 steel welds, were given

further attention as chemical composition nearby internal defects was further investigated.

Variations in Chemical Composition

For DP20, Fig. 11 shows six X-ray compositional maps captured at a weld center, and three horizontal line scans across the maps for the major alloying elements. In addition to voids and cracks along the weld centerline, Fig. 11 shows that the most abundant element, manganese, was most distinctively microsegregated. Its redistribution within the microstructure revealed a fine columnar substructure that grew from the fusion line to the weld centerline. Close examination of the map and line scan of manganese indicates periodic depletion and accumulation every 10 to 20 mm. This microstructural feature alone can be well explained by the classic Scheil's model (Ref. 15), where the manganese-lean regions would be first to solidify and the manganese-rich regions last. Manganese profiles could thus be used to track the solidification substructure.

The line scan of Fig. 11 shows that the peaks for manganese, silicon, and chromium were superimposed. Unlike manganese, chromium distribution was quite uniform, as explained by the iron-chromium partitioning coefficient (nearly one) (Ref. 30). Although zinc was also fairly well dispersed throughout the fusion zone, Fig. 11 raises the possibility of zinc buildup near voids; an observation that is well justified by zinc and iron's limited mutual solubility, and zinc's property to remain liquid long after iron has solidified. In Fig. 11, note that the regions of high X rays for carbon, silicon, and oxygen not only correlated with one another, but were also aligned with the solidification substructure (revealed by the microsegregated manganese). Another important feature is that all three elements were clearly identified in the larger voids, thereby suggesting that they were probably in the form of carbides and silica particles left by the sample preparation. By tracking these last three elements, microscopic voids could be also revealed. In Fig. 10, recall that sulfur, calcium, and potassium were detected in microscopic voids and cracks; an observation that first suggested that these elements could be linked to the formation of internal defects. In this section, we observe that only the contribution of zinc to the formation of internal defects could not be ruled out yet.

Spot Weld Interfacial Fracture

Internal Defects

The numerous weld fracture surfaces

made available by this study were finally examined, as a last attempt to link fracture characteristics, microstructure, and composition. Figure 12A is a low-magnification secondary electron image of a typical weld interfacial fracture in DP20. In welds with sizeable voids, like in Fig. 12A, the possibility that defects such as voids influenced fracture was not dismissed, knowing that voids notoriously decrease spot weld properties (Refs. 15, 31). Figure 12B is a high-magnification view of the large round void of Fig. 12A. The fine dendrites at its surface present additional strong evidence that this void resulted from solidification shrinkage. Also, the cracks at its perimeter indicate that shrinkage caused sufficient tension to split the fine interlocked dendrites apart; i.e., induce a cracking that this time could not be linked to a local change in chemical composition, as was found in Fig. 11. For the intermediate region between the void and the edge of the weld, Fig. 12C shows that a substantial part of the weld exhibits the characteristic microvoids of a ductile fracture, in spite of the high hardness values (Fig. 9) associated with the martensite microstructures (Fig. 10E). Figure 12D shows that brittle fracture by cleavage also occurred, particularly on the side of the weld (i.e., HAZ) where the microstructure was the hardest — Fig. 9.

As for the zinc expulsion, the weld button diameter, and the type of weld fracture, the effects of current, force, and time on the shrinkage voids were all investigated for both steels. Quantitative results to compare voids in DP18 and DP20 are provided first in Fig. 13, which like Fig. 14, was constructed after estimating projected areas of all sizeable voids seen on the interfacial fracture surfaces. Figure 13 clearly shows that the percentage of the fused area covered by the voids was greater in DP20 than in DP18, a feature that is also in line with the greater susceptibility of DP20 welds toward interfacial fracture.

Figure 13 shows that increasing the weld time, thus the weld diameter, reduces the percentage area made by voids in the fusion zone, and thus any contribution voids might have to fracture. Figure 14 confirms these results by showing that an increase in weld diameter, as achieved by raising the current, also decreased the voids rapidly and eliminated weld interfacial fracture (beyond 12 kA). Of the two process variables in Fig. 14, weld force affected most distinctively the relative importance of voids. Voids were reduced dramatically at 1200 lb (5.3 kN) and 1700 lb (7.6 kN), where they were nearly nonexistent. This contrasted with the 20% of the fusion zone they covered at 600 lb (2.7 kN).

Despite evidence that voids could be controlled by process parameters, and in particular reduced by high forces, we found no indication that voids directly caused interfacial fracture. However, we proved that voids and sheet thickness were related by showing that more voids were present in the thicker steel — Fig. 13.

Crack Initiation

Among all fracture surfaces, we discovered that those associated to abnormally fast weld schedules (e.g., 24 kA and 5-cycle weld time) provided a new explanation for spot weld fracture in DP600 steels. Unlike the welds examined previously, the chisel testing of welds made with high currents and extremely short current pulses produced buttons with uncommon characteristics. Figure 15A–F detail one of those welds. First, note the presence of several large eccentric voids, including two on the right of Fig. 15A that appear to be superimposed. Figure 15B, for a part of the fusion zone periphery, shows an abrupt separation between a ductile region with microvoids, and a dendritic solidification structure. Typical characteristics of ductile fracture are also visible in Fig. 15C, as are those of a cleavage brittle fracture. Also, carbon-rich inclusions (likely carbides) were frequently detected in the ductile regions, where they were found deep inside microvoids. Their concentrations were not quantified, since they would have improbably explained DP20's greater weld interfacial fracture susceptibility.

The microstructure shown in Fig. 15D revealed another characteristic feature of these welds made with abnormally fast schedules. Figure 15D is a high-magnification view of the crack that was seen in Fig. 15B. In Fig. 15D, a heavy coating of zinc, confirmed by EDS, is seen on dendrites. Zinc was also encountered for the microconstituent of glassy appearance of Fig. 15E. EDS measurements revealed that its composition matched that of an iron-zinc spinel; i.e., FeZn_2O_4 , a phase we however did not try to validate. In Fig. 15F, where part of the circular void of Fig. 15A is depicted, zinc was also found quite homogeneously distributed over its surface. The fact that zinc was found at dendrites and voids simply confirms that solidification cracking occurred. This cracking, best revealed in Fig. 15D, can be well understood from the binary phase diagram with iron (Ref. 30). The Fe-Zn phase diagram indicates that zinc rejection from the iron solid solution stabilizes a zinc-rich liquid at temperatures as low as the zinc melting temperature; i.e., a perfect condition for cracking to occur, even under normal shrinkage conditions. Although this crack-

ing is clearly detrimental to the welds, we found that chisel-testing zinc-infiltrated welds had consistently produced buttons; an example that demonstrated that chisel testing, and other mechanical tests alone would be inappropriate for these particular welds.

Conclusions

1) The two DP600 steels were successfully resistance spot welded to produce welds resisting interfacial fracture during chisel testing. Low currents (<10 kA), extended weld times (>25 cycles), and high weld forces (>900 lb, or 4.0 kN) promoted weld button formation by producing large fusion zones and occasionally deep (but acceptable) electrode indentations. The greater susceptibility of the DP20 steel to produce weld interfacial fracture was considered to be the results of its thicker gauge (2.0 mm) compared to the DP18 steel (1.8 mm).

2) As explained by carbon equivalents, weld fusion zones in DP600 steels contained mainly martensite, and weld microstructures in the DP18 steel were harder than in the DP20 steel. The dominant effect of sheet thickness was demonstrated by the fact that 1.8-mm-thick DP180 steel showed lower susceptibility to weld interfacial fracture than the thicker DP20 steel, despite its higher carbon equivalent number.

3) Galvanized coatings generally have insignificant effects on weld fracture. However, decreasing weld time and increasing weld current (not typical in production) resulted in zinc ingestion into the fusion zone, which caused solidification cracks. In this investigation, ingestion of zinc was observed at the same time type of fracture changed from one type to the other.

4) Shrinkage voids, recognizable by their dendritic surface morphology, were observed in many welds. High current, long weld time, and high weld force all helped reduce shrinkage voids. Shrinkage voids were less pronounced in the thinner DP18 steel, which also had lower susceptibility for weld interfacial fracture.

Acknowledgments

The authors would like to acknowledge Chris Chen, Alexander Turley, and David Sigler from General Motors for providing frequent valuable discussions. Technical support from Bob Cubic for the scanning electron microscopy and Rich Valdo for the microprobe analysis are also deeply appreciated.

References

1. ULSAB-AVC Consortium, Technical Transfer Dispatch #6 (Body Structure Materials), May 26, 2001.

2. Krauss, G. 1990. *Steels: Heat Treatment and Processing Principles*, Materials Park, Ohio, ASM International.
3. Svenson, L. E., and Larsson, J. K. 2002. *Steel World*, 7: 21–26.
4. Marya, M., and Gayden, X. Q. 2005. *Welding Journal* (in press) Part II of this study.
5. Rathbun, R. W., Matlock, D. K., and Speer, J. G. 2003. *Welding Journal* 79(8): 207-s to 218-s.
6. Militsky, M., Pakalnins, Jiang, C., and Thompson, A. K. 2003. SAE Technical Paper 2003-01-0520.
7. Ghosh, P. K., Gupta, P. C., Ramavtar, A., and Jha, B. K. 1991. *Welding Journal* 71(1): 7-s to 14-s.
8. Ghosh, P. K., Gupta, P. C., Avtar, R., and Jha, B. K. 1990. *ISIJ International* 30(3): 233–240.
9. General Motors Engineering Standards, Automotive Resistance Spot Welding, GM 4488M, Aug. 1995.
10. Japanese Industrial Standard, JIS Z 3140 — *Method of Inspection for Spot Welds*, 2000.
11. Auhl, J. R., and Patrick, E. P. 1994. SAE Technical paper 940160.
12. Saito, T. 1983. *Welding Technique* 31(4): 27.
13. Takcchi, H., and Akisue, O. 1985. *Proceedings of International Conference on HSLA Steels: Metallurgy and Applications*, Beijing, People's Republic of China, pp. 977–984, ASM International.
14. Saito, T., and Ichiyama, Y. 1996. *Welding International* 10(2): 117–123.
15. Olson, D. L., Edwards, G. R., Liu, S., and Frost, R. 1993. *ASM Handbook*, Vol. 6, Welding, Brazing and Soldering, Materials Park, Ohio, ASM International.
16. Devilliers, L., Kaplan, D., and Saint-Martin, P. S. 1986. *Soudage et Techniques Connexes* 40(11-12): 387–395.
17. Babu, S., Goodwin, G. M., Rohde, R. J., and Sielen. 1998. *Welding Journal* 77(6): 249-s to 253-s.
18. Lee, A., and Nagel, G. L. 1988. SAE Technical Paper 880277.
19. Quanfeng, S., Zhang, W., and Bay, N. 2005. *Welding Journal* 84(5): 73-s to 76-s.
20. Harlin, N., Jones, T. B., and Parker, J. D. 2003. *Journal of Materials Processing Technology* 143/144: 448–453.
21. Zhang, S. 1997. *International Journal of Fracture* 88: 167–185.
22. Hess, W. F., and Childs, W. J. 1947. *Welding Journal* 26(4): 712-s to 723-s.
23. Cunningham, A., Legeman, M. L., and Short, B. E. 1966. *Welding Journal* 45(7): 305-s to 313-s.
24. Gould, J. E. 1987. *Welding Journal* 67(1): 1s-10s.
25. Feng, Z., Babu, S. S., Santella, M. L., Riemer, B.W., and Gould, J. E. 1998. *Proceedings of 5th International Conference on Trends in Welding Research*, Pine Mountain, Ga., ASM International.
26. Pan, N., and Sheppard, S. D. 2003. *Engineering Fracture Mechanics* 70: 671–684.
27. Marya, M., Hector, L. G., Gayden, X. Q., and Wang, K. 2005. Paper accepted for publication in *Journal of Manufacturing Engineering, Transactions of ASME*.
28. Zhou, M., Zhang, H., and Hu, S. J. 2003. *Welding Journal* 62(4): 72-s to 77-s.
29. Pook, L. P. 1975. *International Journal of Fracture* 11: 173–176.
30. Baker, H., and Okamoto, H. 1992. *ASM Handbook*, Vol. 3, Alloy Phase Diagrams, ASM International.
31. Gear, A., Westgate, S. A., Kueze, J. C., and Ehrstron, J. C. 1999. *Welding Journal* 78(3): 80-s to 86-s.

WELDING JOURNAL

Instructions and Suggestions for Preparation of Feature Articles

Text

- approximately 1500–3500 words in length
- submit hard copy
- submissions via disk or electronic transmission — preferred format is Mac but common PC files are also acceptable
- acceptable disks include floppy, zip, and CD.

Format

- include a title
- include a subtitle or “blurb” highlighting major point or idea
- include all author names, titles, affiliations, geographic locations
- separate paper into sections with headings

Photos/Illustrations/Figures

- glossy prints, slides, or transparencies are acceptable
- black and white and color photos must be scanned at a minimum of 300 dpi
- line art should be scanned at 1000 dpi
- photos must include a description of action/object/person and relevance for use as a caption
- prints must be a minimum size of 4 in. x 6 in., making certain the photo is sharp
- do not embed the figures or photos in the text
- acceptable electronic format for photos and figures are EPS, JPEG, and TIFF. TIFF format is preferred.

Other

- illustrations should accompany article
- drawings, tables, and graphs should be legible for reproduction and labeled with captions

- references/bibliography should be included at the end of the article

Editorial Deadline

- January issue deadline is November 18
- February issue deadline is December 18
- March issue deadline is January 18
- April issue deadline is February 17
- May issue deadline is March 20
- June issue deadline is April 19
- July issue deadline is May 17
- August issue deadline is June 19
- September issue deadline is July 19
- October issue deadline is August 18
- November issue deadline is September 18
- December issue deadline is October 17

Suggested topics for articles

- case studies, specific projects
- new procedures, “how to”
- applied technology

Mail to:

Andrew Cullison
Editor, Welding Journal
550 NW LeJeune Road
Miami, FL 33126
(305) 443-9353, x 249; FAX (305) 443-7404
cullison@aws.org